Materials & Design 227 (2023) 111712

Contents lists available at ScienceDirect

Materials & Design

journal homepage: www.elsevier.com/locate/matdes

Cochlea-inspired tonotopic resonators

Vinícius F. Dal Poggetto [a], Federico Bosia [b], David Urban [c], Paolo H. Beoletto [b], Jan Torgersen [d], Nicola M. Pugno [a,e], Antonio S. Gliozzi [b,*]

[a] Laboratory for Bio-inspired, Bionic, Nano, Meta Materials & Mechanics, Department of Civil, Environmental and Mechanical Engineering, University of Trento, 38123 Trento, Italy
[b] DISAT, Politecnico di Torino, 10129 Torino, Italy
[c] Department of Electronic Systems, Norwegian University of Science and Technology, NO-7491 Trondheim, Norway
[d] Technical University of Munich, TUM School of Engineering and Design, Department of Materials Engineering, Chair of Materials Science, Boltzmannstr. 15, 85748 Garching, Germany
[e] School of Engineering and Materials Science, Queen Mary University of London, Mile End Road, London E1 4NS, United Kingdom

HIGHLIGHTS

- A novel design for a tonotopic resonator based on a cochlea-inspired spiral is proposed.
- The structure can discriminate the frequency content of elastic waves without the use of sub-wavelength resonators.
- The concept is validated using numerical simulations and experimental measurements using a 3D printed structure.
- The tonotopic behavior can also be inverted for appropriate parameter ranges and boundary conditions.
- The obtained tonotopic features can be used in applications such as non-destructive testing.

GRAPHICAL ABSTRACT

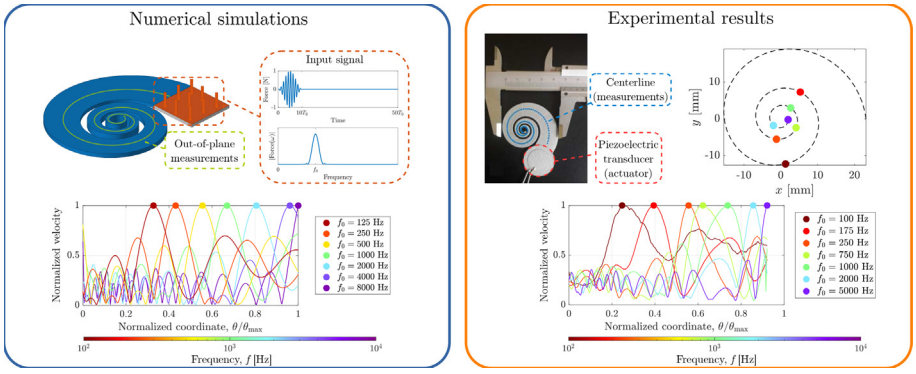

ARTICLE INFO

Article history:
Received 19 November 2022
Revised 24 January 2023
Accepted 7 February 2023
Available online 9 February 2023

Keywords:
Bioinspired structures
Elastic waves
Cochlea
Tonotopy
Eigenmode analysis

ABSTRACT

The cochlea has long been the subject of investigation in various research fields due to its intriguing spiral architecture and unique sensing characteristics. One of its most interesting features is tonotopy, the ability to sense acoustic waves at different spatial locations based on their frequency content. In this work, we propose a novel design for a tonotopic resonator, based on a cochlea-inspired spiral, which can discriminate the frequency content of elastic waves without the use of sub-wavelength resonators. The structure is the result of an optimization process to obtain a uniform distribution of displacement maxima along its centreline for frequencies spanning nearly two-decades, while maintaining a compact design. Numerical simulations are performed to demonstrate the concept and experimental measurements to validate it on a 3D printed structure. The resulting frequency-dependent distribution is also shown to be a viable means to discriminate signals with various frequency components. We also show that for appropriate parameter ranges, the tonotopic behaviour can be inverted, i.e., lower frequencies can be made to concentrate in narrower regions, as happens in the real cochlea. The harnessed tonotopic features can be used as a fundamental principle to design structures with applications in areas such as non-destructive testing and vibration attenuation.

1. Introduction

Among the various sensory organs developed in nature over the course of evolution [1], the cochlea is certainly one of the most fas-

* Corresponding author.
E-mail address: antonio.gliozzi@polito.it (A.S. Gliozzi).

https://doi.org/10.1016/j.matdes.2023.111712
0264-1275/

cinating [2]. This coiled structure possesses unique characteristics which allow mammalians to perceive sounds in wide frequency and amplitudes ranges, comprising nearly ten octaves and 120 decibels [3]. As one of the many examples of naturally occurring spiral structures [4], the cochlea can be approximately modelled by considering a logarithmic spiral description, first presented by Dürer [5], which can be used to investigate the influence of geometrical features on its frequency-dependent characteristics [6]. Beyond the obvious advantages offered by structural coiling in terms of packing, the cochlea also possesses tonotopic characteristics, i.e., where the intensity of the mechano-transduction responsible for converting sound energy into neural impulses varies with the location of peak excitation [7]. Such space-dependent detection of mechanical signals based on their frequency content provides unique frequency detection attributes that are essential for hearing [8].

The design concepts present in the cochlea are also of considerable interest in the field of bioinspired metamaterials, usually employing locally resonant structures able to mimic the tonotopy observed in the cochlea [9–11]. The use of locally resonant structures [12] is widespread in the context of wave manipulation ever since the seminal work presented by Liu et al. [13] opened new possibilities for the development of locally resonant phononic crystals [14,15], thus leading to superior control over elastic waves typically associated with phenomena occurring at sub-wavelength dimensions [16,17]. Examples include one- [18–20], two- [21–24], and three-dimensional applications [25–28].

Although the frequency range associated with local resonance phenomena is typically narrow, the combination of several elements with variable resonant frequencies can be used to create a rainbow effect able to encompass a wider frequency range [29,30]. This effect is typically achieved through the manipulation of the group velocity of traveling waves, which decreases until it reaches a zero value at distinct spatial locations [31,32]. This approach, however, presents considerable limitations, since to achieve effects over a wide frequency range, a large number of elements with distinct resonant frequencies needs to be combined [33]. Also, the typical linear structures tend to be impractical in terms of packing, so that the use of coiled structures is a viable option in the case of acoustic waves [34], but to the best of our knowledge, no similar designs were attempted considering elastic waves propagating in a solid medium. Therefore, current tonotopic solutions based on graded resonators suffer the drawbacks of being restricted to a narrow frequency range while typically being bulky.

The numerical and experimental results presented herein demonstrate how a cochlea-inspired structure can be used as a highly compact element with tonotopic features and tailored resonant frequencies able to span a wide frequency range without relying on resonating elements. The proposed structure can also expand the possibilities of wave manipulation and control, with relevant technological potential in the field of use involving mechanical vibrations, such as in sensing applications [35], energy harvesting [36–40], and noise reduction through the manipulation of multiple band gaps [41–43].

The paper is organized as follows. In Section 2, the geometrical model for the development of the cochlea-inspired resonator is presented, along with relevant metrics which are useful to investigate the spatial distribution of out-of-plane displacement maxima according to the variation of natural frequencies, i.e., the tonotopic modal profile. The numerical and experimental results illustrating the tonotopic behaviour of the proposed curved structure are presented in Section 3. Concluding remarks are presented in Section 4.

2. Models and methods

The cochlea-inspired curved structure is here modelled by sweeping a rectangular cross-section $b(\theta) \times h(\theta)$ (width and height, respectively) along a centreline curve, C, described in a cylindrical coordinate system (r_C, θ, z_C) (see Fig. 1a). The mass density of the structure is taken as constant.

A logarithmic spiral can be written in these coordinates as [6]

$$r_C(\theta) = r_0 e^{k_r \theta/\theta_{\max}},\ z_C = z_C(\theta),\ \theta \in [0,\ \theta_{\max}], \tag{1}$$

where r_0 is the initial radius of the spiral, $k_r \in \mathbb{R}^*$, represents the constant polar slope of the spiral, and $\theta_{\max} = n_T 2\pi$ is the maximum angular coordinate for a number n_T of turns of the cochlea. Similarly, the cross-section dimensions of the cochlea, $b = b(\theta)$ and $h = h(\theta)$, can be written as

$$b(\theta) = b_0 e^{k_b \theta/\theta_{\max}},\ h(\theta) = h_0 e^{k_h \theta/\theta_{\max}}, \tag{2}$$

where b_0 and h_0 represent, respectively, the initial width and height of the cochlea cross-section, and $k_b \in \mathbb{R}$ and $k_h \in \mathbb{R}$ are respectively associated with the variation of the width and height. An example of a cochlea constructed using this approach is shown in Fig. 1b.

Planar cochleae are represented by the simplification $z_C(\theta) = 0$, whose volume can be calculated using Eqs. (1) and (2) as

$$V = r_0 b_0 h_0 \alpha, \tag{3}$$

where $\alpha = (e^{k_r+k_b+k_h} - 1)\theta_{\max}/(k_r + k_b + k_h)$can be regarded as a dimensionless shape factor. The gap in the radial direction between two adjacent turns is given by

$$\Delta_r(\theta) = r_i(\theta) - r_e(\theta + 2\pi), \tag{4}$$

where $r_i(\theta) = r_C(\theta) - b(\theta)/2$ and $r_e(\theta) = r_C(\theta) + b(\theta)/2$ are the inner and outer radii of the cochlea, respectively. Although the condition $\Delta_r(\theta) = 0$ is theoretically possible, it implicates in surface contact and manufacturing issues. Thus, the condition of no overlapping is achieved for $\Delta_r(\theta) > 0, \theta \in [0, (n_T - 1)2\pi]$, which can be related with a minimum gap value ($\Delta_r^{\min}$) and combined with Eqs. (1) and (2), yielding the condition

$$\Delta_r(\theta) = r_0 e^{k_r \theta/\theta_{\max}}\left(1 - e^{k_r/n_T}\right) - (b_0/2)e^{k_b \theta/\theta_{\max}}\left(1 + e^{k_b/n_T}\right) \geqslant \Delta_r^{\min}. \tag{5}$$

Thus, for a given fixed volume V, geometric parameters $\{k_r, k_b, k_h, n_T, h_0\}$, and using Eqs. (3) and (5), the quantities b_0 and r_0 can be determined to give a minimum gap $\Delta_r^{\min}$ in the radial direction, thus ensuring that overlapping does not occur (i.e., the cochlea does not self-intersect, see Fig. 1c).

The arc length of planar cochleae can be computed using the line integral over the radius function in Eq. (1), which, for the case of $z_C = 0$, leads to the centreline normalized coordinate $s \in [0, 1]$, described as

$$s(\theta) = \frac{e^{k_r \theta/\theta_{\max}} - 1}{e^{k_r} - 1}. \tag{6}$$

The cross-section dimensions of the cochlea can also be expressed in terms of the normalized coordinate s using Eq. (6):

$$\begin{aligned} b(s) &= b_0\left[1 + s\left(e^{kr} - 1\right)\right]^{k_b/k_r}, \\ h(s) &= h_0\left[1 + s\left(e^{kr} - 1\right)\right]^{k_h/k_r}, \end{aligned} \tag{7}$$

thus indicating the explicit dependence of b (h) on the ratio k_b/k_r (k_h/k_r), which can be varied to tune the geometric parameters of the spiral.

The set of eigenmodes associated with the resulting structure can be summarized by considering the displacements in a given direction. Out-of-plane direction displacements ($u_z = u_z(\theta, r, z, \omega)$)

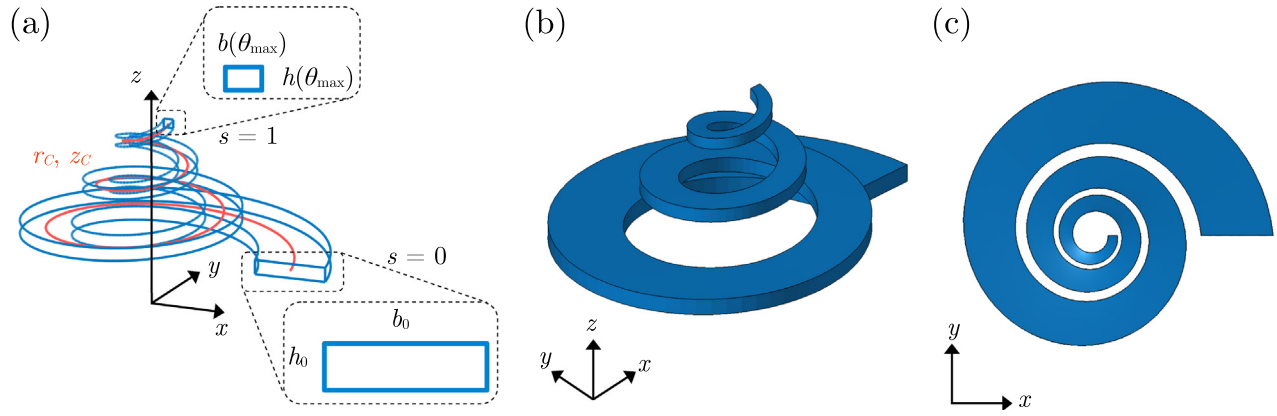

Fig. 1. Model of the cochlea-inspired curved structure. (a) The rectangular cross-section ($b(\theta) \times h(\theta)$) is swept along the curve C described in the cylindrical coordinate system (r_C, θ, z_C), creating a variation between the initial cross-section ($b_0 \times h_0$) and the final cross-section ($b(\theta_{max}) \times h(\theta_{max})$). An example of a cochlear structure constructed using this approach is shown in (b) perspective and (c) top views, respectively.

are chosen due to a biological motivation, since such displacements are analogous to the direction in which the cochlea basilar membrane is coupled with the surrounding fluid, thus being the type of displacements mainly occurring in both flexural and torsional modes. An associated quadratic displacement mean over the cross-section (mean displacement for short), U, can be computed over its transverse directions (r and z) for an eigenmode with the resonant frequency ω, written as

$$U(\theta, \omega) = \frac{1}{A} \int_A |u_z(\theta, r, z, \omega)|^2 \, dr \, dz, \tag{8}$$

where A is the cross-section at coordinate θ, which can be calculated for each eigenmode previously normalized with respect to its largest computed displacement. The quantity $U(\theta, \omega)$ can be computed for a set of resonant modes of a given frequency range of interest, thus yielding a tonotopic modal profile ($U = U(\theta, \omega)$) for this frequency range. The (non-) tonotopic modal profile for a straight structure is discussed and presented in Supplementary Fig. S1 for the sake of comparison.

3. Results

3.1. Optimized tonotopy

Numerical results are computed considering the material properties of a polymer used for 3D printing processes (Solflex SF650, W2P Engineering GmbH), with Young's modulus $E = 2.5$ GPa, Poisson's ratio $\nu = 0.33$, and mass density $\rho = 1150$ kg/m^3. The frequency range of interest is restricted to $[f_{min}, f_{max}] = \left[10^2, 10^4\right]$ Hz, thus encompassing a two-decade range. For the considered material properties and an initial thickness of $L_z = 1$ mm, the smallest flexural wavelength at f_{max} is equal to $\lambda_{min} = \left(EL_z^2/12(1-\nu^2)\rho\right)^{1/4} (2\pi/f_{max})^{1/2} = 16.8$ mm.

The geometries and distribution of mean out-of-plane displacement maxima are computed using the finite element method, considering isoparametric hexahedral elements with linear elastic behavior [44–46]. To obtain the curved structures, an initially straight, regular node grid is mapped into a curved geometry according to the parameters to generate the volume described by Eqs. (1), (2), and (4). The $+y$ and $-y$ faces are mapped into the inner ($r_C(\theta) - b(\theta)/2$) and outer ($r_C(\theta) + b(\theta)/2$) faces, respectively, while the $-z$ and $+z$ faces are mapped into the lower ($-h(\theta)/2$) and upper ($+h(\theta)/2$) faces of the curved structure, respectively. Likewise, the x-coordinates of the initially straight solid element are mapped on to the θ coordinate using the linear relation $\theta(x) = (x/L_x)\theta_{max}$.

The presented quadratic displacement mean metric (see Eq. (8)) is approximated for the use with the finite element discretization considering the sum in the radial and vertical directions, i.e.,

$$U(s, \omega) = \frac{1}{n_r n_z} \sum_r \sum_z u_z^*(s, r, z, \omega) \, u_z(s, r, z, \omega), \tag{9}$$

where n_r and n_z are the number of nodes considered in the finite element model in the radial and vertical directions for a given $s(\theta)$ coordinate, respectively.

A baseline structure, shown in Fig. 2a, is obtained by considering an initially straight structure with the dimensions $L_x = 180$ mm $> 10\lambda_{min}$ and $L_y = 10$ mm $\approx 0.6\lambda_{min}$. The spiral parameters are set as $k_r = \ln(1/10), k_b = \ln(1/10)$ (thus yielding a reduction to 1/10 of the initial width), $k_h = 0$ (fixed thickness), a minimum gap of $\Delta_r^{min} = 1.0$ mm, and a total of $n_T = 3$ turns. The boundary conditions are considered as clamped at the face with largest width of the cochlea ($\theta = 0$) and free at the other end ($\theta = \theta_{max}$), thus representing the attachment of the structure to an ideally infinitely stiff substrate. The distribution of mean displacement maxima, indicated in Fig. 2b, presents considerable tonotopy, with a noticeable separation between the peak for each mode up to 1.5 kHz (as indicated by the black dashed fitting line), where the bending modes (A and B, Fig. 2c) are clearly distinguishable. Above this frequency, the maximum of each eigenmode occurs at $\theta = \theta_{max}$, thus losing tonotopy. Also, for higher frequencies, higher-order bending modes in the radial direction (which can also be interpreted as torsional in the circumferential direction) may occur (modes C and D, Fig. 2c), thus hindering the desirable clear visualization of tonotopy.

The manipulation of tonotopy can be achieved by varying the geometric parameters that control the curvature, width, and thickness of the cochlea (see Supplementary Fig. S2). If not chosen properly, however, these parameters may lead to prohibitively small features, which can be difficult in terms of manufacturing, thus suggesting that optimal values can be obtained considering practical manufacturing limitations. Therefore, to better evaluate and quantify the level of ideal tonotopy presented by the structure, we propose a metric (Γ) defined as

$$\Gamma(k_b, k_r, k_h, n_T) = \sum_i d_i^2(k_b, k_r, k_h, n_T), \tag{10}$$

where $d_i = |s_i - \overline{\omega}_i|/\sqrt{2}$ represents the distance between the maximum of the mean displacements computed for the i-th out-of-

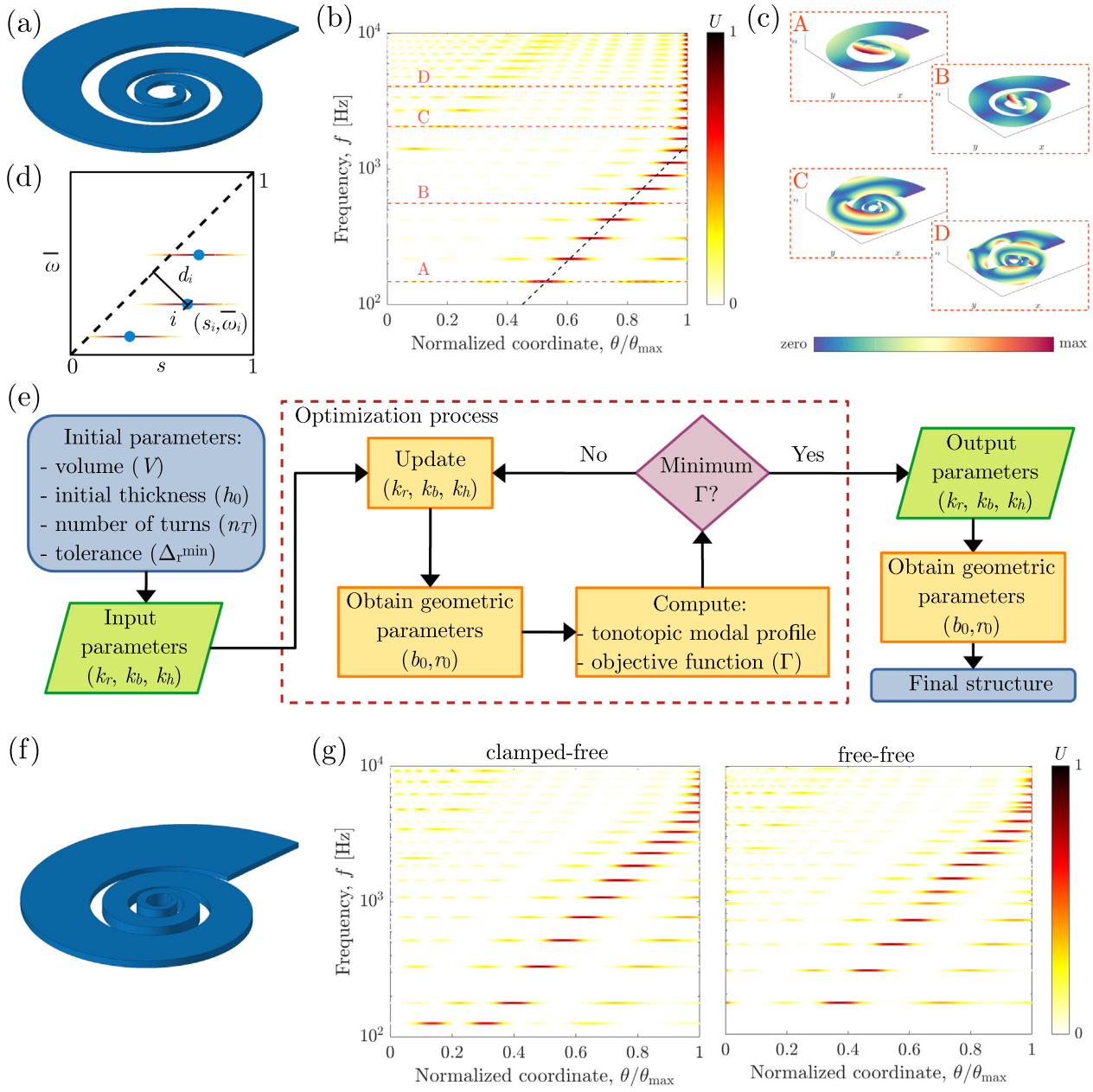

Fig. 2. Initial investigation on the distribution of mean displacement maxima for a baseline design. (a) Structure obtained for $k_r = k_b = \ln(1/10), k_h = 0, \Delta_r^{\min} = 1$ mm, and $n_T = 3$ turns. (b) The modal profile displays noticeable tonotopy up to 1.5 kHz with spatial separation between the peaks of the eigenmodes as their resonant frequencies increase (modes A and B); this separation is hindered at higher frequencies and includes higher order torsional modes (modes C and D). (c) Vibration modes A – D. (d) Illustration of the distance considered in the quantification of tonotopy for the normalized space (s) and frequency ($\overline{\omega}$) coordinates, with the distance d_i between the maximum of the out-of-plane mean displacements for the i-th mode and the $\overline{\omega} = s$ line that represents ideal tonotopy. (e) Schematic of the optimization process, indicating the fixed initial values $(V, h_0, n_T, \Delta_r^{\min})$ and variables in the optimization process (k_r, k_b, k_h), which are used to obtain the geometric parameters (b_0, r_0) and compute the optimization metric (Γ). (f) Obtained structure considering parameters that minimize the metric of tonotopy and (g) its tonotopic modal profile considering clamped-free (at $\theta = 0$ and $\theta = \theta_{\max}$, respectively) and free-free boundary conditions.

plane vibration mode and the $\overline{\omega} = s$ line, as illustrated in Fig. 2d, calculated considering the normalized coordinate s_i and the normalized frequency $\overline{\omega}_i = \log(\omega_i/\omega_{\min})/\log(\omega_{\max}/\omega_{\min})$, for $\omega_{\max} = 2\pi f_{\max}$ and $\omega_{\min} = 2\pi f_{\min}$. The $\overline{\omega} = s$ line is considered as the ideal distribution of modes maxima, since it covers the entire frequency range with an uniform spatial distribution. The overall optimization process is illustrated in the schematic presented in Fig. 2e, which summarizes the initial (fixed) parameters $(V, h_0, n_T, \Delta_r^{\min})$, the parameters which undergo the optimization procedure (k_r, k_b, k_h), and the remaining geometric parameters which are obtained to satisfy the geometric constraints (b_0, r_0) and evaluate the tonotopic modal profile and objective function (Γ). The description of each quantity is given in Section 2. The combination of the objective function and the restrictions on variables k_b, k_r, and k_h yields a constrained nonlinear optimization problem, which is solved using an active set algorithm [47] implemented in Matlab [48] to obtain global optimal solutions.

For the present problem, a fixed number of turns and minimum gap are considered ($n_T = 3$ and $\Delta_r^{\min} = 1.0$ mm), restricting the optimization parameters to $k_r \in [\ln(1/20), \ln(1/2)], k_b \in [\ln(1/20), \ln(1/2)]$, and $k_h \in [\ln(1), \ln(5)]$. The optimization results yield

$k_r = \ln(1/12), k_b = \ln(1/20)$, and $k_h = \ln(5)$. Very similar results were obtained when considering normalized $\theta/\theta_{\max}$ coordinates instead of s in the optimization metric given by Eq. (10). It is interesting to notice that k_b is equal to the lower boundary of the variable, yielding a quasi-linear width decrease in the s-coordinate ($k_b/k_r = 1.2$, see Eq. (7)), while the height increase is steeper, equal to the upper boundary of the variable ($k_h/k_r = -0.65$, see Eq. (7)). The resulting structure is shown in Fig. 2f, and the corresponding distribution of mean displacement maxima is shown in Fig. 2g for the clamped-free and free-free boundary conditions, indicating a significant improvement in tonotopy.

3.2. Inverted tonotopic modal profile

It is known that in the actual cochlea, low frequencies are mostly detected in the inner part (apex), and high frequencies in the outer part (base) [49]. The opposite happens for elastic wave propagation in the structures considered up to this point. However, this is not necessarily true in all cases. Consider, for example, a structure obtained through the same previously described process, but stiffer at its outer edge ($s = 0$) and more flexible at the inner edge ($s = 1$), thus inducing, respectively, high- and low-frequency resonant frequencies in these regions.

To this end, let the geometrical control parameters be $k_r = \ln(1/5), k_b = \ln(2)$, and $k_h = \ln(1/5)$. Also, all edges of the structure are considered as clamped to account for the stiffness of the surrounding medium supporting the basilar membrane in the cochlea. In this case, we also consider larger dimensions to obtain resonant frequencies comparable with the previous examples, using $L_x = 500$ mm, $L_y = 100$ mm, $L_z = 2$ mm, $\Delta_r^{\min} = 1$ mm, and $n_T = 3$ turns. These parameters result in the structure presented in Fig. 3a, occupying an area of approximately 567×502 mm^2. The associated tonotopic modal profile is shown in Fig. 3b, with a limit curve (s^*, dashed green line) indicating the location of local maxima, which confines the elastic energy at the region delimited by $s > s^*$ for each resonant frequency. Vibration modes marked as A–D are displayed in Fig. 3c, indicating that the locations of maximum displacement move from the inner to the outer region of the cochlea as the frequency increases, as expected. For lower frequencies, the points of maxima are quite noticeable.

Although this type of structure may be interesting for certain applications and demonstrates the versatility of the proposed approach, it suffers from drawbacks such as (i) the considerable presence of empty spaces in the planar design, thus leading to a low efficiency in the use of space, (ii) the large dimensions associated with the final structure, and (iii) the poor discrimination between maxima, which possibly hinders the use of the structure in sensing applications.

3.3. Demonstration of tonotopy

The tonotopy of the structure achieved through an optimization procedure is also demonstrated by a numerical simulation where transient signals are considered. The obtained structure, shown in Fig. 2e, is attached to a square platform of dimensions 16.2×16.2 mm^2, to which a Gaussian modulated sinusoidal signal is applied, as depicted in Fig. 4a.

For the definition of the input signal, a set of fundamental frequencies (f_0) is considered. For each case, the duration of the burst consists of 10 periods, i.e., $T_b = 10/f_0$, while the total duration of the signal is $T_s = 50/f_0$ (see the inset of Fig. 4a). The fundamental frequencies are chosen as $f_0 = \{125, 250, 500, 1000, 2000, 4000, 8000\}$ Hz. Time-domain transient analyses based on the Newmark method [45] are performed, and the resulting out-of-plane velocity values (v_z) computed for the centreline of the sample (green line in Fig. 4a). A Fast Fourier Transform (FFT) is applied considering each separate θ coordinate and plotted using distinct colors for the obtained frequency components ($\hat{v}_z$), as shown in Fig. 4b for each central frequency. For the first input frequency, the maximum of out-of-plane mean displacements is located close to $\theta/\theta_{\max} = 0.34$, thus resembling the results computed considering the clamped end (Fig. 2f). Each computed maximum (highlighted by a coloured dot) shifts to higher values of θ as the input frequency increases, thus clearly demonstrating the effect of tonotopy.

To verify the tonotopy of the designed cochlea and the feasibility of its potential use as a frequency selective device, we also performed an experimental realization of the spiral structure obtained by the numerical optimization process. The structure was printed on a commercial 3D-DLP printer (Solflex SF650, W2P Engineering GmbH) using polymeric resin Solflex Tech Though (from the same manufacturer) with the same mechanical properties as considered in the numerical simulations. The printer is equipped with an UV-LED emitting at a wavelength of 385 nm and with a specified power density of 8 ± 0.5 mW/cm^2. The nominal lateral resolution is 50 μm and the printer supports layer thicknesses ranging from 25 to 200 μm. Here, the design was sliced into layers of 50 μm, each exposed for 1.5 s, leading to a dose of 12 mJ/cm^2 per layer. The parts were oriented with their (r, θ)-plane parallel to the printing platform such that the slicing was performed along the z-axis and were printed standing on a removable support structure to increase the bottom surface smoothness. After printing, the parts

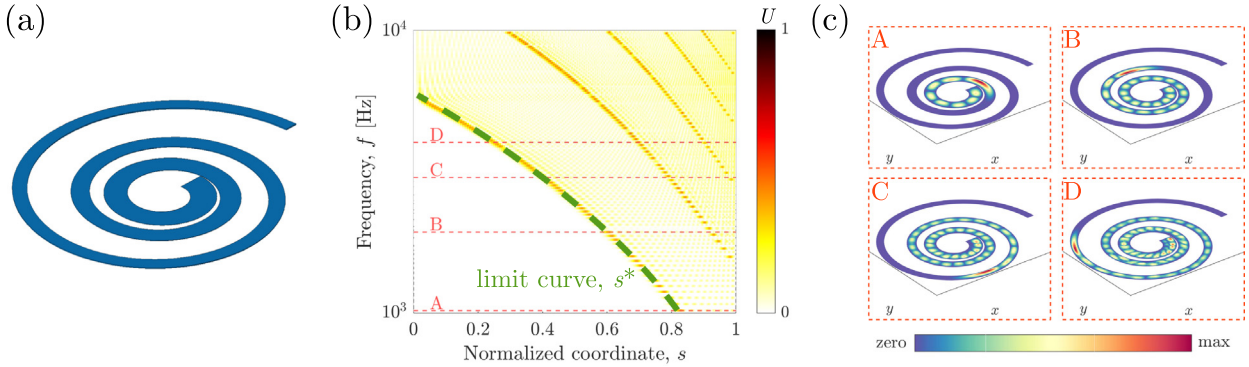

Fig. 3. Initial investigation on the distribution of mean displacement maxima for a baseline design. (a) The structure obtained considering $k_r = k_h = \ln(1/5), k_b = \ln(2), \Delta_r^{\min} = 1$ mm, and $n_T = 3$ turns yields an (b) inverted tonotopic modal profile that shows a limit curve (s^*, dashed green line) confining the significant out-of-plane elastic energy to regions delimited by $s > s^*$. (c) Vibration modes A–D, marked in (b), indicating a decreasing confinement of energy as the resonant frequencies increase.

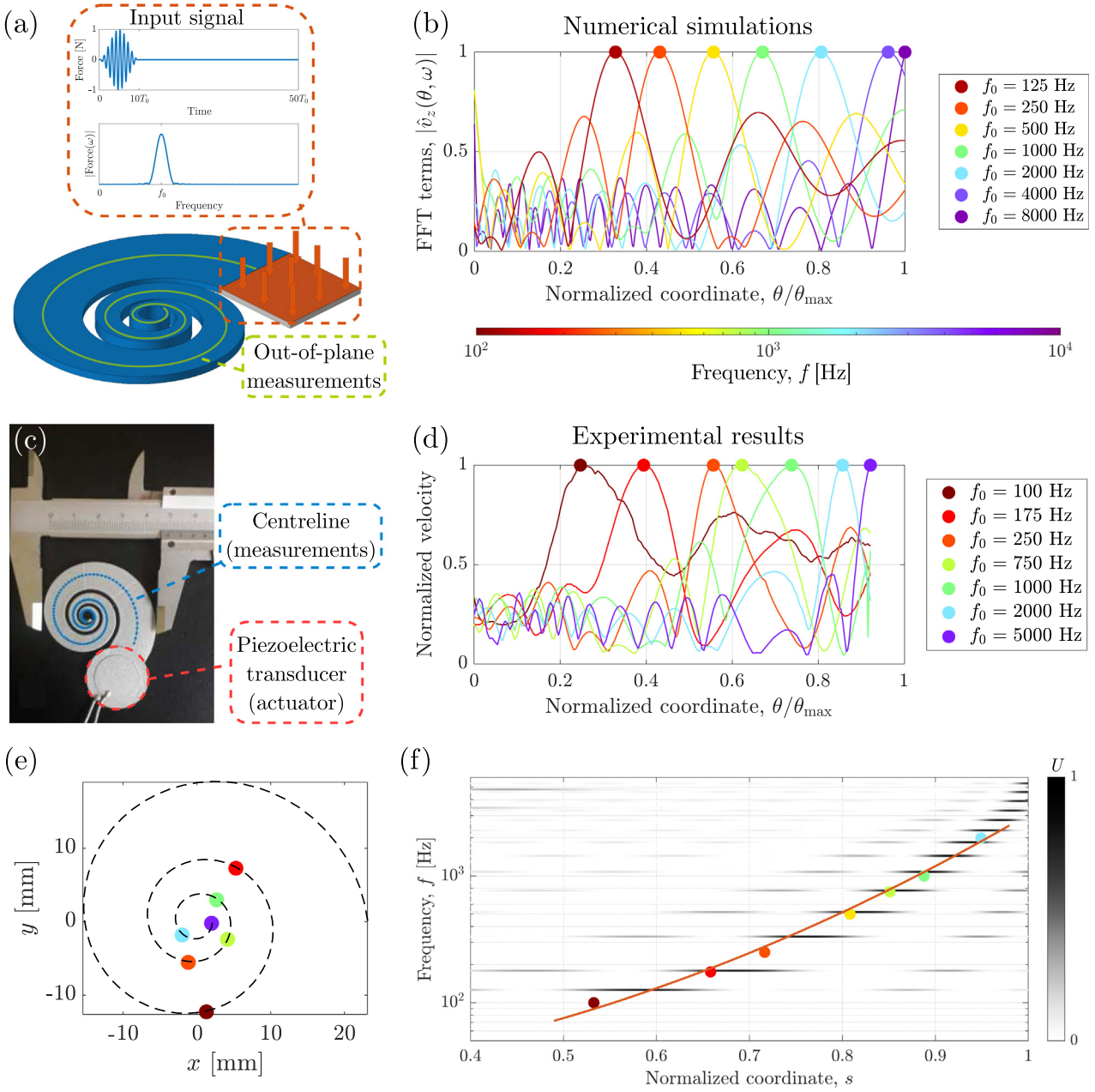

Fig. 4. Numerical simulation and experimental results demonstrating the tonotopy of the considered spiral structure using transient signals. (a) The optimized spiral structure is attached to a square platform where an input force is applied on the red area, and out-of-plane velocities are computed at the cochlea centre, depicted by the green line. Inset: example of employed input signal, consisting of 10 periods contained in a Hanning window and a total of 50 periods. (b) The effect of tonotopy is demonstrated by observing the varying spatial location of the maximum of the frequency components to increasing θ values as the input frequency f_0 increases. (c) Sample and experimental set-up, showing the force input element (piezoelectric transducer, in red) and the location of the measured out-of-plane velocities along the cochlea centreline (in blue). (d) Measured normalized velocity amplitude detected at different points for various central frequencies (f_0), reported as a function of the angular position ($\theta/\theta_{\max}$) in the cochlea centreline. (e) Representation of each signal maximum along the measured portion of the cochlea centreline. (f) Distribution of the maxima along the s coordinate, overlaid with the previously obtained tonotopic frequency distribution in the clamped-free configuration (Fig. 2f).

were washed with Isopropyl Alcohol (IPA), then fully immersed in IPA and sonicated twice for 5 min in an ultrasonic bath (USC200TH, VWR International). Finally, they were UV-post-cured for 1 h in a PHOTOPOL Analog UV-curing unit (Dentalfarm Srl), providing all-around illumination in the wavelength range 320–450 nm.

The experimental setup was also similar to the one considered in the numerical simulations. A piezoelectric transducer, with a diameter of 20 mm and negligible weight with respect to the entire structure, was glued to the external edge of the printed cochlea resonator (see red circle in Fig. 4c). A Gaussian shaped signal with varying central frequency (f_0) was injected with an arbitrary function generator (Agilent 33500), amplified by a factor 20 by a liner amplifier (FLC Electronics, A400DI), and applied to the piezoelectric transducer. The central frequency f_0 of the signals varied in the range $\Delta f_0 = [100, 5000]$ Hz, with a burst duration of $T_b = 10/f_0$. The experiment was repeated for each frequency f_0, recording the response of the structure in 200 points along the centreline of the cochlea (see blue dots in Fig. 4c), using a laser vibrometer (Polytec, OFV-505) to detect the out-of-plane velocities on the surface of the sample.

The results of the experiment are reported in Fig. 4d, where the normalized amplitude of the velocity signals detected at various

different points are reported as a function of the angular position on the cochlea centreline. The different coloured lines, which use the same frequency-based color coding as presented in Fig. 4b, represent the responses of the structure for different values of the central frequency f_0 of the exciting burst and correspond, respectively, to $100, 175, 250, 750, 1000, 2000$, and 5000 Hz. Results show that the maximum (highlighted by a coloured dot) moves along the cochlea centreline starting from the outer part (maximum radius) to the apex (minimum radius), where higher frequencies are detected. The maxima are well resolved in space, as highlighted by reporting the position of the maximum amplitude on the cochlea centreline (see Fig. 4e), and each maximum is unique for a fixed frequency along the cochlea, thus proving the tonotopy of the structure.

By plotting the logarithm of the central frequency as a function of the position of the maximum in the normalized s coordinate for a given set of central frequencies, it is possible to recognize a clear correlation with the tonotopic modal profile previously presented in Fig. 2f; for greater clarity, results are overlaid in Fig. 4f. Also, a functional dependence between the central frequency and its location in the cochlea centreline can be estimated by an exponential fit of the form $\tilde{f}(s) = ge^{kl(\theta)^2}$ (see Eq. (6)), with $g = 22$ Hz and $k = 0.7$ m^{-2}. In this case, the frequency range is reduced to $[100, 2000]$ Hz to allow for single fit, instead of adopting a piecewise function. Also, an additional measurement is performed at $f_0 = 500$ Hz (yellow point in Fig. 4b) to confirm its closeness to the exponential fit. This fit may allow to identify the optimal position for the detection on the structure of a certain frequency in the range Δf_0.

3.4. Sensing applications

Having assessed the validity of the tonotopic effect on the optimized spiral structure, we now propose a numerical experiment to demonstrate its possible use in sensing and non-destructive testing applications. For this purpose, a $216 \times 16 \times 1$ mm^3 beam is attached to the previously designed cochlea and platform structure. The beam is then excited with an out-of-plane point force at 40 mm from the edge of the platform, located at its upper face and applied at its centre. Points P_1, P_2, P_3, and P_4, corresponding to the frequencies of 250 Hz, 500 Hz, 1 kHz, and 2 kHz are chosen as outputs. As these frequencies are not necessarily resonant frequencies, the location of the points at the central line of the cochlea are determined by a linear interpolation of the peaks presented in Fig. 2f for the θ coordinate, resulting in the angles $\theta/2\pi = 1.3, \theta/2\pi = 1.6, \theta/2\pi = 2.0$, and $\theta/2\pi = 2.4$, respectively. The resulting structure is presented in Fig. 5a. Distinct input forces with single frequency components and the same amplitudes are applied for a total of 10 periods and a Hanning window (see the inset in Fig. 4a), while the output signals are computed for a total of 20 periods. The normalized acceleration output values are presented in Fig. 5b. In each case, the single-frequency input signal generates the strongest response at the corresponding output point, i.e., 250 Hz for point P_1, 500 Hz for point P_2, 1 kHz for point P_3, and 2 kHz for point P_4. Furthermore, although excitation signals at lower frequencies still produce a considerable response at the high-frequency output points (e.g., the output at P_4 is appreciable even for the 250 Hz input signal), this effect is much less pronounced at higher frequencies. In particular, for an input frequency of 2 kHz, the output accelerations at points P_1 – P_3 are considerably smaller than at P_4, which can be explained by the localization of out-of-plane mean displacements of higher frequency modes.

As a second application, let us now consider the problem of determining the frequency content of a signal containing multiple harmonics, which may derive, for instance, from nonlinearities. Let us define such a signal as $F_n(t) = \sum_{i=0}^{n} w_i \sin\left(2^i \omega_0 t\right)$, for $\omega_0 = 2\pi f_0$, which is applied as the input force of the structure shown in Fig. 5a, considering the fundamental frequency $f_0 = 250$ Hz and 3 additional harmonics (500 Hz, 1 kHz, and 2 kHz). For the sake of numerical evaluation, we consider $w_0 = 1, w_1 = 1/2^2, w_2 = 1/2^3$, and $w_3 = 1/2^4$. The representation of signals F_0, F_1, F_2, and F_3, applied for a total of 10 periods relative to the f_0 frequency are shown in the first row of Fig. 5c. The normalized acceleration outputs at points P_1 – P_4, computed considering the single frequency signal F_0 and labelled respectively as a_1 – a_4, are shown in the second row of Fig. 5c, where all output signals oscillate with the same frequency. As the number of harmonics is increased, a differential acceleration quantity, Δa_i, can be computed at the i-th point as $\Delta a_i = a_i - a_i^{\text{ref}}$, where a_i^{ref} is taken as the reference case (1 harmonic) shown in Fig. 5c. The corresponding variation for each differential acceleration is shown in Figs. 5c for the inputs F_1 – F_3, respectively, where it is possible to notice a variation in the differential acceleration of each point as the number of harmonics used to compose the excitation signal increases.

The differential acceleration can also be used to compute the integral $I_i = \int \Delta a_i^2 \, dt$, thus indicating an increase in the acceleration associated to the i-th point. The results are indicated in Table 1 for each distinct excitation, where it may be noticed that (i) for 2 harmonics (F_1), I_2 is clearly larger than the other quantities, which is also indicated in the second row of Fig. 5c; (ii) for 3 harmonics (F_2), I_3 presents a substantial increase; (iii) for 4 harmonics (F_3), I_4 presents the most noticeable increase. Thus, it is possible to demonstrate that an increase in the number of harmonics can be detected by each of the corresponding output points through a metric associated to the measured acceleration.

4. Conclusions

In summary, we have proposed a new efficient and compact design for cochlea-inspired tonotopic structures, created by sweeping a rectangular area along a logarithmic spiral curve. The resulting structure presents a distribution of out-of-plane displacement maxima along its centreline, which can be modified by exploiting the geometrical parameters that control the curvature, width, and height of the structure, thus achieving a tunable tonotopic effect which does not rely on the use of sub-wavelength resonant elements. Although torsional modes (in the radial direction) can occur for higher frequencies, bending modes (in the circumferential direction) dominate the vibration mode spectrum.

The proposed device differs from traditional signal processors and FFT analyzers as its operation is based solely on its mechanical response to a signal, thereby eliminating the need for electronic components. This makes it an ideal choice for applications that require low power consumption in sensing and vibration signal processing, such as in the Internet of Things (IoT) [50,51]. Its ability to separate frequency components into multiple output channels without consuming battery power makes it a valuable addition to wireless sensors as a signal processor. Additionally, the parallel processing of multiple outputs at high speed makes it a suitable option for control systems that require a fast response to external excitations, such as in automotive suspension control systems [52] or robotic assembly applications [53]. In the context of speech recognition [54,55], this device could serve as an efficient preprocessing tool, converting the auditory signal into recognizable patterns, and thus enhancing the overall performance of speech recognition systems that benefit from frequency-related data. As neuromorphic computing [56,57] aims to move towards hardware implementations of several tasks of machine learning, this device

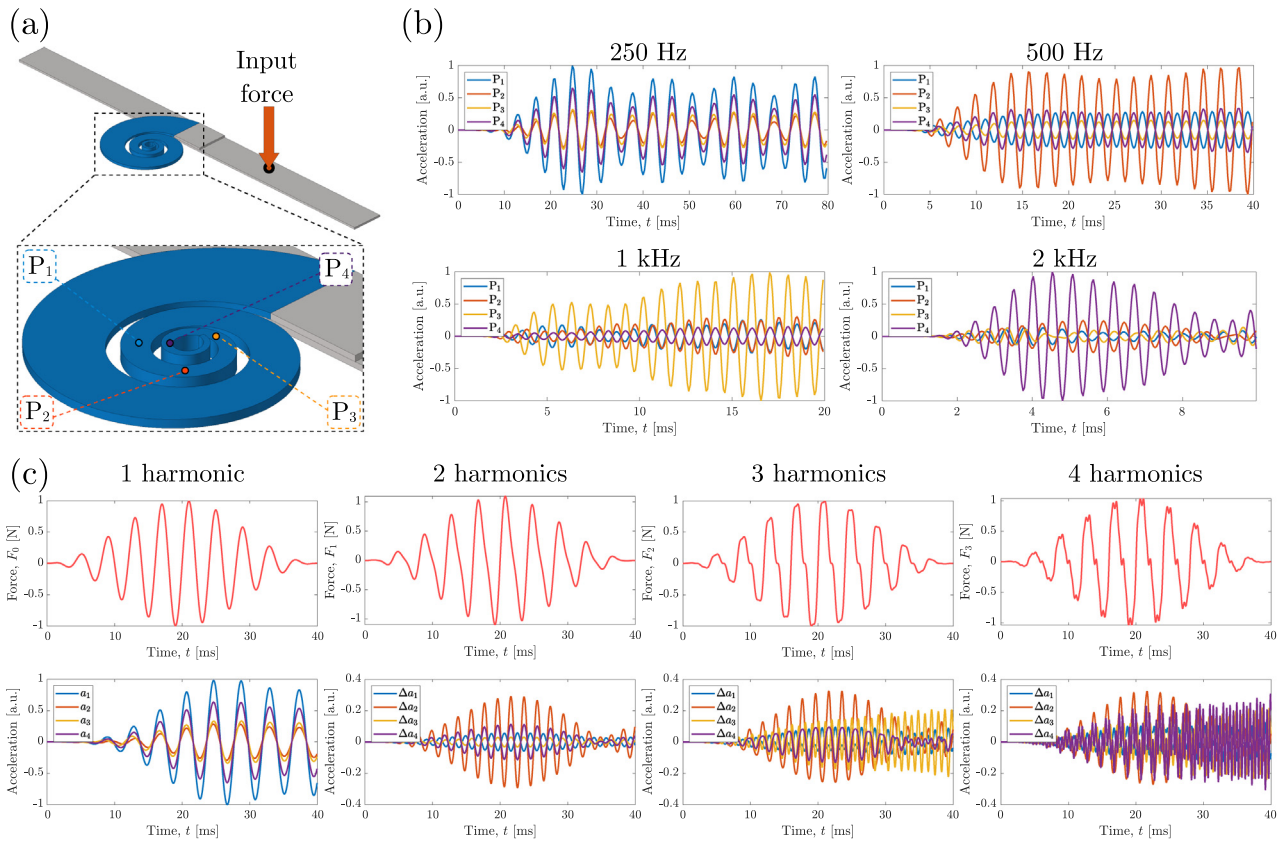

Fig. 5. Sensing application for the cochlea-inspired resonator as a frequency detection device of waves traveling in a beam. (a) An input force is applied at the upper face of the beam, with output points on the cochlea labelled as P_1, P_2, P_3, and P_4, with increasing θ coordinates. (b) Computed out-of-plane accelerations, normalized with respect to the largest acceleration value for each input frequency: 250 Hz, 500 Hz, 1 kHz, and 2 kHz. Maximum corresponding amplitudes are detected at P_1, P_2, P_3, and P_4, respectively. (c) Input force (first row) and normalized acceleration outputs (second row) considering input signals with increasing number of harmonics, namely 1 harmonic (250 Hz), 2 harmonics (250 and 500 Hz), 3 harmonics (0.25, 0.5, and 1 kHz), and 4 harmonics (0.25, 0.5, 1, and 2 kHz).

Table 1
Integral over time for square of differential accelerations.

I_i [a.u.]	Excitation F_1 (2 har.)	F_2 (3 har.)	F_3 (4 har.)
$I_1 \times 10^{-3}$	0.0279	0.0539	0.0767
$I_2 \times 10^{-3}$	0.5691	0.5868	0.5935
$I_3 \times 10^{-3}$	0.0076	0.3460	0.3586
$I_4 \times 10^{-3}$	0.0840	0.0894	0.5411

could also serve as a low-power pre-processing tool and fulfil a role similar to that of the inner ear, by which it is biologically inspired.

The resulting tonotopy can be optimized by distributing the modal displacements maxima along a linear spatial distribution that realizes ideal tonotopy, i.e., uniformly distributed resonant frequencies along the structure. Using this procedure, we were able to design and fabricate a structure which displays a uniform distribution of mean displacement maxima over nearly two decades, as demonstrated both numerically and experimentally. The potential use of such structures in sensing applications, possibly including output channels located along its centreline, was also numerically demonstrated for signals with single and multiple frequency components.

The presented results open new possibilities, through targeted designs, for applications of tonotopic bioinspired materials in energy harvesting, non-destructive testing, and vibration attenuation.

5. CRediT authorship contribution statement

ASG conceived the manuscript idea; VFDP performed the numerical analyses and simulations; DU and JT performed the manufacturing of samples; ASG and PHB performed the experiments on manufactured samples; NMP and ASG supervised the work; VFDP, FB, and ASG wrote the first version of the manuscript. All authors contributed to the discussion of the manuscript and gave approval to the final version.

6. Data availability statement

The data that support the findings of this study are available from the corresponding author upon reasonable request.

Data availability

Data will be made available on request.

Declaration of Competing Interest

The authors declare that they have no known competing financial interests or personal relationships that could have appeared to influence the work reported in this paper.

Acknowledgments

VFDP, FB, PHB, NMP, and ASG are supported by the EU H2020 FET Open "Boheme" Grant No. 863179. JT and DU acknowledge the Norwegian University of Science and Technology for funding the PhD fellowship under project number 81148180.

Appendix A. Supplementary material

Supplementary data associated with this article can be found, in the online version, at https://doi.org/10.1016/j.matdes.2023.111712.

References

[1] F. Bosia, V.F. Dal Poggetto, A.S. Gliozzi, G. Greco, M. Lott, M. Miniaci, F. Ongaro, M. Onorato, S.F. Seyyedizadeh, M. Tortello, N.M. Pugno, Optimized structures for vibration attenuation and sound control in nature: A review, Matter 5 (10) (2022) 3311–3340.
[2] P. Dallos, R.R. Fay, The Cochlea, Vol. 8, Springer Science & Business Media, 2012.
[3] L. Robles, M.A. Ruggero, Mechanics of the mammalian cochlea, Physiol. Rev. 81 (3) (2001) 1305–1352.
[4] M. Livio, The golden ratio: The story of phi, the world's most astonishing number, Crown, 2008.
[5] A. Dürer, Underweysung der Messung, mit dem Zirckel und Richtscheyt, in Linien, Ebenen unnd gantzen corporen, Nüremberg 1525.
[6] D. Manoussaki, R.S. Chadwick, D.R. Ketten, J. Arruda, E.K. Dimitriadis, J.T. O'Malley, The influence of cochlear shape on low-frequency hearing, P. Natl. Acad. Sci. USA 105 (16) (2008) 6162–6166.
[7] M. LeMasurier, P.G. Gillespie, Hair-cell mechanotransduction and cochlear amplification, Neuron 48 (3) (2005) 403–415.
[8] S.J. Lighthill, Biomechanics of hearing sensitivity, J. Vib. Acoust. 113 (1) (1991) 1–13.
[9] F. Ma, J.H. Wu, M. Huang, G. Fu, C. Bai, Cochlear bionic acoustic metamaterials, Appl. Phys. Lett. 105 (21) (2014) 213702.
[10] F. Ma, J.H. Wu, M. Huang, S. Zhang, Cochlear outer hair cell bio-inspired metamaterial with negative effective parameters, Appl. Phys. A 122 (5) (2016) 1–8.
[11] M. Rupin, G. Lerosey, J. de Rosny, F. Lemoult, Mimicking the cochlea with an active acoustic metamaterial, New J. Phys. 21 (9) (2019) 093012.
[12] C. Goffaux, J. Sánchez-Dehesa, A.L. Yeyati, P. Lambin, A. Khelif, J.O. Vasseur, B. Djafari-Rouhani, Evidence of fano-like interference phenomena in locally resonant materials, Phys. Rev. Lett. 88 (22) (2002) 225502.
[13] Z. Liu, X. Zhang, Y. Mao, Y.Y. Zhu, Z. Yang, C.T. Chan, P. Sheng, Locally resonant sonic materials, Science 289 (5485) (2000) 1734–1736.
[14] M.S. Kushwaha, P. Halevi, G. Martinez, L. Dobrzynski, B. Djafari-Rouhani, Theory of acoustic band structure of periodic elastic composites, Phys. Rev. B 49 (4) (1994) 2313.
[15] V. Laude, Phononic crystals, de Gruyter, 2020.
[16] A. Colombi, R.V. Craster, D. Colquitt, Y. Achaoui, S. Guenneau, P. Roux, M. Rupin, Elastic wave control beyond band-gaps: shaping the flow of waves in plates and half-spaces with subwavelength resonant rods, Front. Mech. Eng. 3 (2017) 10.
[17] A.O. Krushynska, M. Miniaci, F. Bosia, N.M. Pugno, Coupling local resonance with bragg band gaps in single-phase mechanical metamaterials, Extreme Mech. Lett. 12 (2017) 30–36.
[18] Y. Xiao, J. Wen, G. Wang, X. Wen, Theoretical and experimental study of locally resonant and bragg band gaps in flexural beams carrying periodic arrays of beam-like resonators, J. Vib. Acoust. 135 (4) (2013).
[19] Y. Xiao, J. Wen, D. Yu, X. Wen, Flexural wave propagation in beams with periodically attached vibration absorbers: band-gap behavior and band formation mechanisms, J. Sound Vib. 332 (4) (2013) 867–893.
[20] V.F. Dal Poggetto, A.L. Serpa, J.R.F. Arruda, Optimization of local resonators for the reduction of lateral vibrations of a skyscraper, J. Sound Vib. 446 (2019) 57–72.
[21] Y. Xiao, J. Wen, X. Wen, Flexural wave band gaps in locally resonant thin plates with periodically attached spring–mass resonators, J. Phys. D: Appl. Phys. 45 (19) (2012) 195401.
[22] E.J.P. Miranda Jr., E.D. Nobrega, A.H.R. Ferreira, J.M.C. Dos Santos, Flexural wave band gaps in a multi-resonator elastic metamaterial plate using Kirchhoff-love theory, Mech. Syst. Signal Pr. 116 (2019) 480–504.
[23] V.F. Dal Poggetto, A.L. Serpa, Flexural wave band gaps in a ternary periodic metamaterial plate using the plane wave expansion method, J. Sound Vib. 495 (2021) 115909.
[24] G. Aguzzi, C. Kanellopoulos, R. Wiltshaw, R.V. Craster, E.N. Chatzi, A. Colombi, Octet lattice-based plate for elastic wave control, Sci. Rep. 12 (1) (2022) 1–14.
[25] S.J. Mitchell, A. Pandolfi, M. Ortiz, Metaconcrete: designed aggregates to enhance dynamic performance, J. Mech. Phys. Solids 65 (2014) 69–81.
[26] L. D'Alessandro, E. Belloni, R. Ardito, A. Corigliano, F. Braghin, Modeling and experimental verification of an ultra-wide bandgap in 3d phononic crystal, Appl. Phys. Lett. 109 (22) (2016) 221907.
[27] W. Witarto, S.J. Wang, C.Y. Yang, J. Wang, Y.L. Mo, K.C. Chang, Y. Tang, Three-dimensional periodic materials as seismic base isolator for nuclear infrastructure, AIP Adv. 9 (4) (2019) 045014.
[28] V.F. Dal Poggetto, A.L. Serpa, Elastic wave band gaps in a three-dimensional periodic metamaterial using the plane wave expansion method, Int. J. Mech. Sci. 184 (2020) 105841.
[29] G.J. Chaplain, J.M. De Ponti, G. Aguzzi, A. Colombi, R.V. Craster, Topological rainbow trapping for elastic energy harvesting in graded Su-Schrieffer-Heeger systems, Phys. Rev. Appl. 14 (5) (2020) 054035.
[30] J.M. De Ponti, L. Iorio, E. Riva, R. Ardito, F. Braghin, A. Corigliano, Selective mode conversion and rainbow trapping via graded elastic waveguides, Phys. Rev. Appl. 16 (3) (2021) 034028.
[31] J. Zhu, Y. Chen, X. Zhu, F.J. Garcia-Vidal, X. Yin, W. Zhang, X. Zhang, Acoustic rainbow trapping, Sci. Rep. 3 (1) (2013) 1–6.
[32] M. Alshaqaq, C. Sugino, A. Erturk, Programmable rainbow trapping and band-gap enhancement via spatial group-velocity tailoring in elastic metamaterials, Phys. Rev. Appl. 17 (2) (2022) L021003.
[33] H. Meng, N. Bailey, Y. Chen, L. Wang, F. Ciampa, A. Fabro, D. Chronopoulos, W. Elmadih, 3D rainbow phononic crystals for extended vibration attenuation bands, Sci. Rep. 10 (1) (2020) 1–9.
[34] X. Ni, Y. Wu, Z.-G. Chen, L.-Y. Zheng, Y.-L. Xu, P. Nayar, X.-P. Liu, M.-H. Lu, Y.-F. Chen, Acoustic rainbow trapping by coiling up space, Sci. Rep. 4 (1) (2014) 1–6.
[35] Y. Pennec, Y. Jin, B. Djafari-Rouhani, Phononic and photonic crystals for sensing applications, Adv. Appl. Mech. 52 (2019) 105–145.
[36] M. Carrara, M.R. Cacan, J. Toussaint, M.J. Leamy, M. Ruzzene, A. Erturk, Metamaterial-inspired structures and concepts for elastoacoustic wave energy harvesting, Smart Mater. Struct. 22 (6) (2013) 065004.
[37] S. Qi, M. Oudich, Y. Li, B. Assouar, Acoustic energy harvesting based on a planar acoustic metamaterial, Appl. Phys. Lett. 108 (26) (2016) 263501.
[38] J.M. De Ponti, A. Colombi, R. Ardito, F. Braghin, A. Corigliano, R.V. Craster, Graded elastic metasurface for enhanced energy harvesting, New J. Phys. 22 (1) (2020) 013013.
[39] J.M. De Ponti, A. Colombi, E. Riva, R. Ardito, F. Braghin, A. Corigliano, R.V. Craster, Experimental investigation of amplification, via a mechanical delay-line, in a rainbow-based metamaterial for energy harvesting, Appl. Phys. Lett. 117 (14) (2020) 143902.
[40] Z. Lin, H. Al Ba'ba'a, S. Tol, Piezoelectric metastructures for simultaneous broadband energy harvesting and vibration suppression of traveling waves, Smart Mater. Struct. 30 (7) (2021) 075037.
[41] Y. Xiao, B.R. Mace, J. Wen, X. Wen, Formation and coupling of band gaps in a locally resonant elastic system comprising a string with attached resonators, Phys. Lett. A 375 (12) (2011) 1485–1491.
[42] Y. Xiao, J. Wen, X. Wen, Broadband locally resonant beams containing multiple periodic arrays of attached resonators, Phys. Lett. A 376 (16) (2012) 1384–1390.
[43] D. Guan, J.H. Wu, L. Jing, N. Gao, M. Hou, Application of a Helmholtz structure for low frequency noise reduction, Noise Control Eng. 63 (1) (2015) 20–35.
[44] R.D. Cook, Concepts and Applications of Finite Element Analysis, Wiley, 2001.
[45] K.J. Bathe, Finite Element Procedures, Prentice-Hall International Series, Prentice Hall, 1996.
[46] A.J.M. Ferreira, MATLAB Codes for Finite Element Analysis: Solids and Structures, Solid Mechanics and Its Applications, Springer, Netherlands, 2010.
[47] S. Wright, J. Nocedal, Numerical optimization, Springer Science 35 (67–68) (1999) 7.
[48] The MathWorks, Inc., MATLAB Optimization Toolbox, Natick, MA, US (2020). https://www.mathworks.com/help/optim/
[49] T. Reichenbach, A.J. Hudspeth, The physics of hearing: fluid mechanics and the active process of the inner ear, Rep. Prog. Phys. 77 (7) (2014) 076601.
[50] D. Jung, Z. Zhang, M. Winslett, Vibration analysis for IoT enabled predictive maintenance, in: in: 2017 IEEE 33rd International Conference on Data Engineering (ICDE), IEEE, 2017, pp. 1271–1282.
[51] J.P. Lynch, K.J. Loh, A summary review of wireless sensors and sensor networks for structural health monitoring, Shock and Vibration Digest 38 (2) (2006) 91–130.
[52] H.E. Tseng, D. Hrovat, State of the art survey: active and semi-active suspension control, Vehicle Syst. Dyn. 53 (7) (2015) 1034–1062.
[53] D.K. Thomsen, R. Søe-Knudsen, O. Balling, X. Zhang, Vibration control of industrial robot arms by multi-mode time-varying input shaping, Mech. Mach. Theory 155 (2021) 104072.
[54] R.V. Sharan, T.J. Moir, Acoustic event recognition using cochleagram image and convolutional neural networks, Appl. Acoust. 148 (2019) 62–66.
[55] F. Abreu Araujo, M. Riou, J. Torrejon, S. Tsunegi, D. Querlioz, K. Yakushiji, A. Fukushima, H. Kubota, S. Yuasa, M.D. Stiles, J. Grollier, Role of non-linear data processing on speech recognition task in the framework of reservoir computing, Sci. Rep. 10 (1) (2020) 1–11.
[56] Y. Usami, B. van de Ven, D.G. Mathew, T. Chen, T. Kotooka, Y. Kawashima, Y. Tanaka, Y. Otsuka, H. Ohoyama, H. Tamukoh, H. Tanaka, W.G. van der Wiel, T. Matsumoto, In-materio reservoir computing in a sulfonated polyaniline network, Adv. Mater. 33 (48) (2021) 2102688.
[57] G. Milano, G. Pedretti, K. Montano, S. Ricci, S. Hashemkhani, L. Boarino, D. Ielmini, C. Ricciardi, In materia reservoir computing with a fully memristive architecture based on self-organizing nanowire networks, Nat. Mater. 21 (2) (2022) 195–202.